IEEE Access
Multidisciplinary | Rapid Review | Open Access Journal

Received 15 March 2023, accepted 27 March 2023, date of publication 29 March 2023, date of current version 3 April 2023.

Digital Object Identifier 10.1109/ACCESS.2023.3262828

RESEARCH ARTICLE

Efficient Radiation Pattern Estimation of Slot Array Antennas Covered With Frequency Selective Surfaces Using Deterministic Ray Tracing

DAEYEONG YOON[1], (Student Member, IEEE), JIHYUNG KIM[2], (Member, IEEE), HOKEUN SHIN[3], (Member, IEEE), DONG-YEOP NA[4], (Member, IEEE), AND YONG BAE PARK[1,5], (Senior Member, IEEE)

[1]Department of AI Convergence Network, Ajou University, Suwon, Gyeonggi 16499, South Korea
[2]Hanwha Systems, Yongin 17121, South Korea
[3]Core Component Technology Team of Mobile Experience, Samsung Electronics, Suwon 16677, South Korea
[4]Department of Electrical Engineering, Pohang University of Science and Technology, Pohang 37673, South Korea
[5]Department of Electrical and Computer Engineering, Ajou University, Suwon, Gyeonggi 16499, South Korea

Corresponding author: Yong Bae Park (yong@ajou.ac.kr)

This work was supported by the National Research Foundation of Korea (NRF) Grant funded by the Korea Government [Ministry of Science and ICT (MSIT)] under Grant 2021R1A4A1030775.

ABSTRACT In this paper, we propose a novel algorithm to compute the radiation pattern of a slot array antenna covered with frequency selective surfaces (FSS) based on ray tracing technique. We observe that the proposed algorithm can greatly reduce computational resources while yielding accurate numerical solutions, compared to cases using standard full-wave and conventional high-frequency approaches. The underlying principle is to combine the image method and physical optics technique. More specifically, the proposed algorithm (i) employs a boundary box that encloses the slot array antenna with FSS to correct phase errors and then (ii) calculates equivalent surface currents flowing on the boundary box. The surface of the boundary box is discretized by regular grids (or boundary meshes) and a ray path reaching each square cell in the boundary meshes is determined based on the image method. After collecting all the rays hitting the boundary meshes, equivalent surface current densities can be computed for the resulting radiation pattern. The proposed algorithm is suited best for dealing with electrically large structures much more efficiently and can advance the existing design process.

INDEX TERMS Ray tracing, image method, radome, array antenna, frequency selective surface (FSS).

I. INTRODUCTION

Rapid advances in radar technology have made it possible to detect enemy weapons early. Conversely, allies are more likely to be detected by the enemy, which may threaten their chances of survival. Therefore, in order to reduce the probability of radar detection, it must be accompanied by stealth techniques, such as radar cross-section (RCS) reduction. Military aircrafts or guided missiles, for instance, are often equipped with high-powered radars to detect targets. However, these high-powered radars that typically involve metallic structures exhibit larger RCS. In this case, frequency selective surfaces (FSS) are widely employed for the RCS reduction [1], [2], [3], [4], [5], [6], [7], [8], [9], [10], [11], [12], [13], [14], [15].

There exist two main configurations for the use of FSS structures in reducing RCS. The first one is to insert FSS structures into a curved radome, called conformal FSS, and the other type is to directly place a planar FSS layer on top of an antenna. A conformal FSS radome is often designed in a

The associate editor coordinating the review of this manuscript and approving it for publication was Giorgio Montisci.

shape that can scatter electromagnetic waves in the reflection band to reduce RCS [7]. However, the overall performance may be degraded by deformations of FSS elements [16], [17]. Moreover, design, fabrication, and maintenance of conformal FSS structures would not be a trivial task in practice. On the other hand, planar FSS structures can achieve the RCS reduction via reflection and absorption characteristics in the stop band [8], [9], [10], [11], [12], [13], [14], [15]. For example, the use of flat FSS structures could improve the stealth performance of naval mast [14], and minimize the antenna gain reduction [15]. In addition, it is much easier to design, fabricate, and maintain planar FSS structures than conformal FSS structures.

There have been a plenty of previous works on electromagnetic analyses of FSS radome structures [1], [2], [3], [4], [6]. The electromagnetic performance of a radome were evaluated by considering multiple reflections of rays from FSS layers in the 2D plane [1]. And in [3] and [6], the radiative properties of a curved radome embedding FSS layers were studied by exploiting the equivalence theorem and modeling curved radome as a tangent surface. Nevertheless, neither methods mentioned in the above considered the phase errors of rays due to the presence of a FSS radome in the near-field zone. If a built-in antenna had a larger Rayleigh distance than the radome's dimension, one could not obtain a correct radiation pattern with the abovementioned methods. Therefore, a new method is needed for cases where planar FSS layers exist in the near-field region.

Typical FSS structures include several hundreds of periodic unit cells. Although the electrical size of each unit cell is subwavelength ($<=0.3\lambda$), fine features embodied in each unit cell should be captured for the accurate evaluation. In addition, the overall size of an antenna covered planar FSS structures is electrically very large. Consequently, the significant amount of computing power is required for the analysis when using full-wave methods, e.g., finite element method (FEM), method of moments (MoM), and mesh modeling process. In this case, one can make the high-frequency approximation and use the ray tracing technique to efficiently calculate the radiation pattern.

There exist two competing approaches in the ray-tracing technique [18], [19], [20], [21], [22], [23], [24], [25], [26], [27], [28]. The first one is the image method popularly used in the propagation channel modeling. It finds the path of reflected and diffracted rays such that electromagnetic environments can be specified with the smaller number of rays [18], [19], [20], [21]. The second approach is the shooting and bouncing ray (SBR) method that computes electromagnetic scattering fields. To do this, it launches numerous of rays from a source and applies physical optics (PO) techniques at the ray reaching point. Being accurate and having various applications including RCS and radome analyses [22], [23], [24], [25], [26], [27], [28]. Structures such as curved surfaces or cavities can be efficiently calculated using the SBR technique. However, for structures that are not complex in shape, such as planes, the image method technique can be calculated more efficiently.

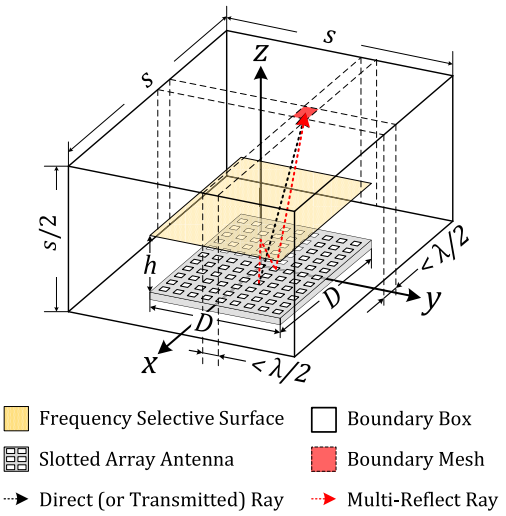

FIGURE 1. Schematic of the proposed method. Equivalent surface current densities can be calculated by collecting all the rays reaching the boundary meshes. Subsequently, one can compute the radiation pattern of the slot antenna.

In this paper, we propose a novel algorithm that can efficiently calculate the radiation pattern of a slot array antenna covered with a planar FSS structure by combining the image method and PO technique. We introduce a boundary box that encloses the slot array antenna and compute equivalent surface currents flowing on the box. The boundary box is discretized by regular grids, and each square cell in the boundary mesh is sized by a half wavelength or less. The ray path from the slot antenna to the boundary mesh is determined by using the image method. After collecting all the rays hitting boundary meshes, equivalent surface currents can be computed from electric and magnetic field values to calculate the resulting radiation pattern. Utilizing the proposed algorithm, we analyze the radiation pattern of 316 slot array antennas covered with a planar FSS layer (square ring slot unit cell). We present all the details about the design and simulation. To verify the proposed algorithm, the results were compared with those by commercial software. We shall demonstrate that the proposed algorithm can greatly reduce computational resources while yielding accurate numerical solution, compared with cases taking standard full-wave and conventional high-frequency approaches (summarized in Table 1).

II. NUMERICAL METHOD

A. OVERVIEW OF OUR METHOD

This section provides a brief overview of the proposed algorithm as shown in the schematic diagram in Fig. 1 The problem we are trying to solve is the FSS placed on top of the slotted array antenna.

Since the rays are generated from each slot, the far field condition for each slot antenna must be satisfied. Therefore, the distance (h) between FSS and array antenna must be larger

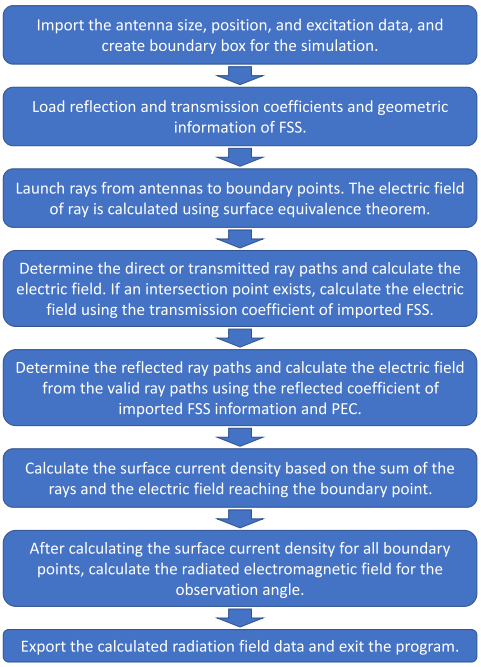

FIGURE 2. Flow chart of the proposed method.

than the far field distance of each slot. In this case, h is 10 mm, and the far field distance of each slot element is 4.2 mm. As in the conventional FSS radome analysis technique [3], [4], [5], [6], the radiation pattern can be calculated by defining the equivalent current on the enclosed surface. However, as mentioned in the introduction, the phase error of the ray from the point source must be corrected. To minimize this phase error, a boundary box (sized by $s \times s \times 0.5s$ m^3) was created. The bounding box is composed of a 2D boundary mesh with each side less than half the wavelength to satisfy the Nyquist sampling theory [29]. To calculate the radiation pattern, it is modeled as a direct wave by connecting the rays from the antenna to the boundary mesh. Then, the image method is used to determine the path of the reflected wave. In the process of determining the path of the reflected wave, an invalid ray path is inspected by searching for intersections, etc. Based on the found reflection and transmission nodes, the electromagnetic field reaching the boundary mesh can be calculated. Based on the ray path reaching the boundary mesh, the PO technique is applied to calculate equivalent surface electric current and magnetic current densities. Afterwards, the radiation pattern is calculated using the surface electric and magnetic currents flowing on the boundary mesh. The flowchart shown in Fig. 2 provides a detailed overview of the steps. Detailed procedures are described in following section.

B. DETERMINE RAY PATH USING IMAGE METHOD

As shown by the dotted arrow in Fig. 1, the rays from the antenna reach each boundary mesh. In this process, it is necessary to determine the direct or transmit ray path (black dotted arrow in Fig. 1) and the multiple reflected rays between the antenna and the FSS (red dotted array in Fig. 1). The direct ray path can be defined with the midpoint of the antenna as the starting point and the boundary mesh as the ending point. The multiple reflection paths between the antenna and FSS can be determined using the image method. The surface currents in a boundary mesh can be calculated by finding the start and end points of each ray and the intersection between the meshes. The detailed process is expressed in two dimensions in Fig. 3, which can be applied in a three-dimensional space.

Fig. 3a is the process of determining the direct and the transmitted ray path. The planar antenna and FSS are imported, and they are divided into a finite plane (mesh) and an infinite plane (Plane). Next, a line segment was drawn between the boundary mesh and the midpoint of the antenna. If the line segment has an intersection with the plane and it is located inside the FSS, it is judged as a transmitted ray. In other cases, it was judged by direct ray path.

Fig. 3b is the process of determining the correct ray path. In order to provide hints for generalized program implementation, the invalid process was first described. The image boundary mesh point (circled 1) which is a symmetry point through FSS plane (FSS symmetry) was created. Then a new image boundary mesh point on the GND plane of circled 1 (FSS-GND symmetry, circled 2) was created. The line segment between the above two points (circled 1, 2) and the antennas was defined and the length was calculated. It is an incorrect path because the length of the calculated line segment is shorter than the length of the direct ray. Next, we describe how to determine the valid ray used in the actual calculation. Similar to the previous process, the image boundary mesh point (circled 3) which is a mirror of point through GND plane (GND symmetry) was created. Then a new image boundary mesh point on the FSS plane of circled 3 (GND-FSS symmetry, circled 4) was created. These line segments are invalid ray paths because they have the same length as the direct ray. It indicates that there is no first-order reflection component. Next, the line segment between the above two points (circled 3, 4) and the antennas was defined and the length was calculated. These line segments are valid ray paths because they are longer than the length of direct ray. It indicates that a secondary reflection component may be present, so an additional step is required to obtain the correct intersection point.

Fig. 3c is the back tracking process to find the intersection point between the ray and meshes. In the previous procedure, we have shown that a point symmetrical to the GND-FSS plane (circled 4) is valid. The back tracking needs to do the flip over the plane again in reverse order (FSS and then GND symmetry) to determine if it's a valid ray. First, the circled 4 and the antenna was defined and the intersection point with the FSS mesh was obtained with box 4, 5, and 6. If there is no intersection with the mesh, it is an invalid ray path and the search ends. Mirrored circled 4 to the FSS plane and moved it to circled 3. Defined a line segment connecting the intersection with the FSS mesh (box 4, 5, 6) and circled3. The intersection between the GND mesh and the above line

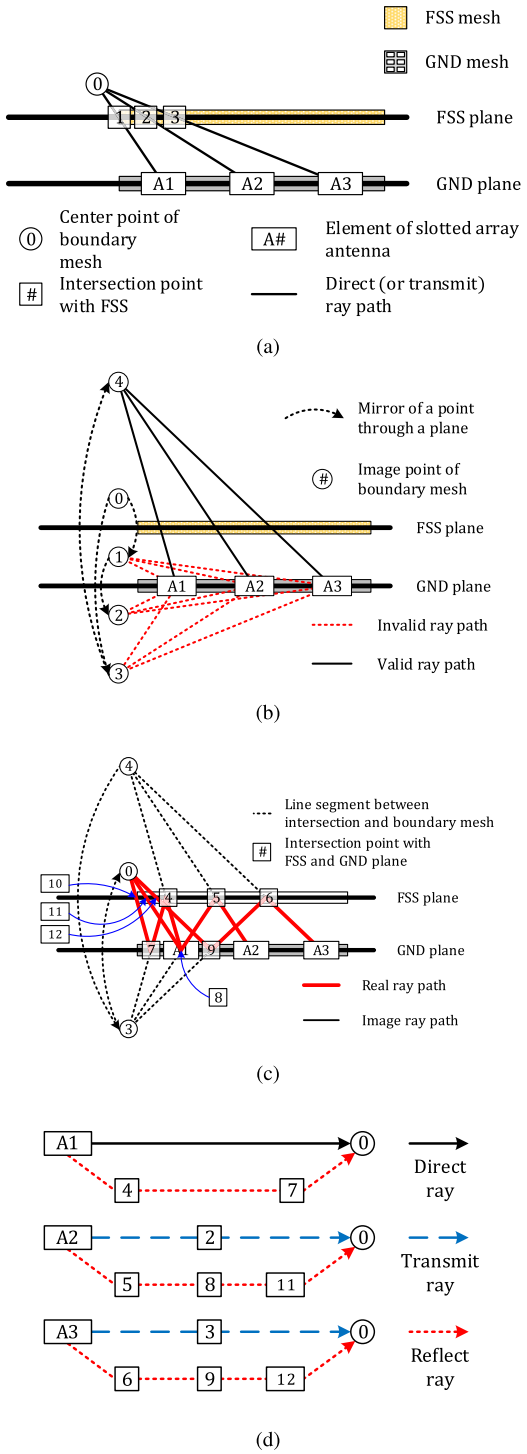

FIGURE 3. The procedure of the proposed method, it can be applied in 3D space. (a) Direct ray path determination (b) Invalid ray detection process (c) Back tracking for reflection path from valid ray path (d) The ray path between the antenna and the boundary mesh.

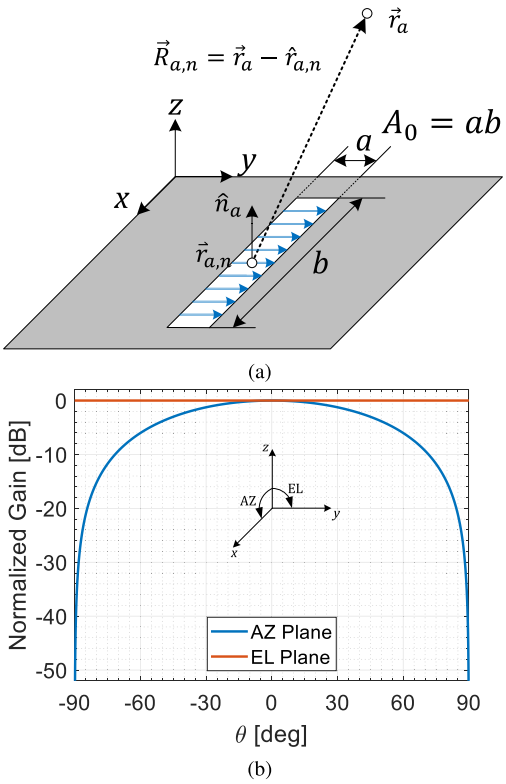

FIGURE 4. Single slot antenna under consideration (a) Geometry (b) Radiation pattern of single slot antenna.

segment was obtained with box 7, 8, and 9. If there is no intersection with GND here, it is an invalid ray path and the search ends. Finally, move circled 3 to circled 0 by mirroring it to the GND plane. The line segment between circled 0 and the intersection of the GND mesh (box 7, 8, 9) was defined, and the intersection with the FSS mesh was calculated with box 10, 11, and 12. If there is no intersection with the FSS mesh (such as box 10), it is a direct wave without propagation inside the FSS. On the other hand, if there is an intersection with the FSS mesh (box 11, 12), it can be judged as a transmitted ray through the FSS.

Fig. 3d is the result of arranging the path of the ray. Two ray paths from each antenna to the boundary mesh were calculated. In addition, two times of reflection and one time of transmission were considered. The propagating electromagnetic field component can be calculated using the normal vector of the intersection surface. In addition, the surface current density in the boundary mesh is calculated from these field component.

C. RAY FIELDS FROM ANTENNA

We considered the case where electromagnetic waves are generated from the slot antenna. The surface electric and magnetic currents $\vec{J}_a$ and $\vec{M}_a$ generated in the slot antenna can be calculated by [5] (See Fig. 4)

$$\vec{J}_a = 0, \quad \vec{M}_a = -2A_0\hat{n}_a \times \vec{E}_a \tag{1}$$

where $\hat{n}_a$ is the normal vector of the slot antenna surface, A_0 is the area of the slot, and $\vec{E}_a$ excited electric field from the feed. Then the electric field radiated $\vec{E}_r$ from the surface magnetic current $\vec{M}_a$ at the center point of the each slot antenna $\vec{r}_{a,n}$ to

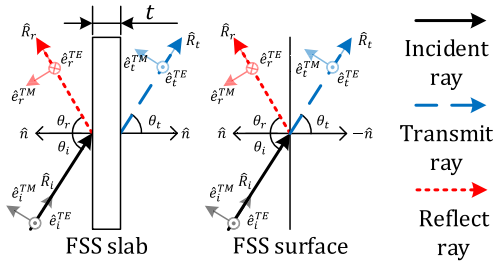

FIGURE 5. Simplification of FSS slab and vector elements of rays.

the target point $\vec{r}_a$ can be calculated by [29]

$$\vec{E}_r(\vec{r}_a) = \frac{jkA_0}{4\pi R_{a,n}}\left[\hat{R}_{a,n} \times \vec{M}_a(\vec{r}_{a,n})\right] e^{-jkR_{a,n}} \tag{2}$$

where $\vec{R}_{a,n}$ is expressed as the target point $\vec{r}_a$ minus the center position of the slot antenna $\vec{r}_{a,n}$, $R_{a,n}$ is the magnitude of $\vec{R}_{a,n}$, $\hat{R}_{a,n}$ is the normalized vector of $\vec{R}_{a,n}$ and the area of slot A_0 is expressed as the product of the width a and length b of the slot. If the path of the ray is obtained as shown in Fig. 3d, the target point can be defined as the points circled 0, and 2, 3, 4, 5, and 6 of box.

D. REFLECT AND TRANSMIT RAY FIELD MODELING

As shown in Fig. 5, 3D FSS slab was approximated as a 2D FSS surface. The properties of FSS were obtained using the commercial software HFSS, which supports periodic structural analysis.

However, since the 3D model is scaled down to 2D, the reflection and transmission phases should be subtracted by the phase propagating in free space of the same thickness. The phase of the FSS surface can be defined from the phase of the FSS slab by

$$\begin{aligned} \angle R_{surf}^{TE,TM} &= \angle R_{slab}^{TE,TM} - \frac{4\pi}{\lambda_0} t\cos\theta_i \\ \angle T_{surf}^{TE,TM} &= \angle T_{slab}^{TE,TM} - \frac{2\pi}{\lambda_0} t\cos\theta_i \end{aligned} \tag{3}$$

where λ_0 is the wavelength in free-space, t is the thickness of the FSS, and θ_i is the incidence angle of plane wave. The electromagnetic field of ray can be divided into transverse electric (TE) and transverse magnetic (TM) polarization components. Each of the TE and TM polarization components can be written as the normal vector of the FSS plane and the propagation component of the ray by

$$\begin{aligned} \hat{e}_i^{TE} &= \frac{\hat{R}_i \times \hat{n}}{|\hat{R}_i \times \hat{n}|}, \quad \hat{e}_i^{TM} = \hat{e}_i^{TE} \times \hat{R}_i \\ \hat{e}_r^{TE} &= -\hat{e}_i^{TE}, \quad \hat{e}_r^{TM} = \hat{R}_r \times \hat{e}_r^{TE} \\ \hat{e}_t^{TE} &= \hat{e}_i^{TE}, \quad \hat{e}_t^{TM} = \hat{e}_i^{TM} \end{aligned} \tag{4}$$

In addition, the incident electromagnetic field ($E_{TE,TM}$) and reflection ($\Gamma_{TE,TM}$) and transmission coefficient ($T_{TE,TM}$)

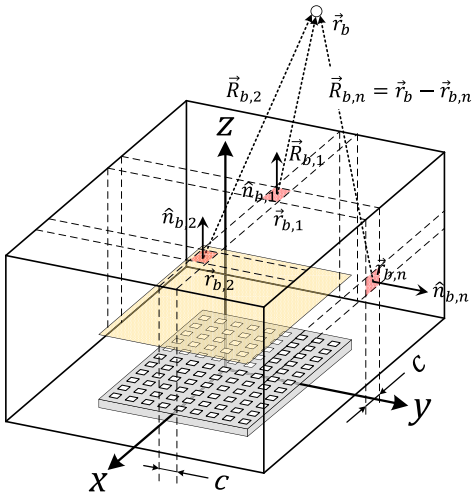

FIGURE 6. Relevant vector quantities needed when calculating scattered fields in boundary grids.

can be defined by

$$\begin{aligned} E^{TE} &= \vec{E}_i \cdot \hat{e}_i^{TE}, \quad E^{TM} = \vec{E}_i \cdot \hat{e}_i^{TM} \\ \vec{E}_r &= \Gamma^{TE} E^{TE} \hat{e}_r^{TE} + \Gamma^{TM} E^{TM} \hat{e}_r^{TM} \\ \vec{E}_t &= T^{TE} E^{TE} \hat{e}_t^{TE} + T^{TM} E^{TM} \hat{e}_t^{TM} \end{aligned} \tag{5}$$

Since only reflected waves are generated in GND, there is no need to consider transmitted waves. Therefore, the field of the reflected wave generated from GND can be calculated by multiplying the reflection coefficient of PEC by -1.

E. EQUIVALENT SURFACE CURRENT DENSITIES ON THE BOUNDARY BOX

It was confirmed in the previous section that the ray component reaching the boundary mesh consists of a direct or transmitted wave (subscript i, t) and a multi-reflected wave (subscript r). Therefore, the surface electric and magnetic current density can be defined as the sum of the electromagnetic field components of the ray reaching the boundary mesh by [29]

$$\begin{aligned} \vec{J}_{b,n}(\vec{r}_{b,n}) &= \hat{n} \times [\vec{H}_{i,t} + \vec{H}_r] \\ \vec{M}_{b,n}(\vec{r}_{b,n}) &= [\vec{E}_{i,t} + \vec{E}_r] \times \hat{n} \end{aligned} \tag{6}$$

where $\hat{n}_b$ is the normal vector at the boundary.

F. RADIATION PATTERN CALCULATION

The radiated electromagnetic field from all boundary meshes to the observation point $\vec{r}_b$ we want to observe can be defined by [29]

$$\begin{aligned} \vec{E}_s(\vec{r}_{b,n}) = \frac{jk}{4\pi}\int_s [&\hat{R}_{b,n} \times \hat{R}_{b,n} \times \vec{J}_{b,n}(\vec{r}_{b,n}) \\ &+ \hat{R}_{b,n} \times \vec{M}_{b,n}(\vec{r}_{b,n})] \frac{e^{-jkR_{b,n}}}{R_{b,n}} ds \end{aligned} \tag{7}$$

where $\vec{r}_{b,n}$ is the center point of boundary mesh, and $\vec{R}_{b,n}$ is difference between the observation point $\vec{r}_b$ and the mesh

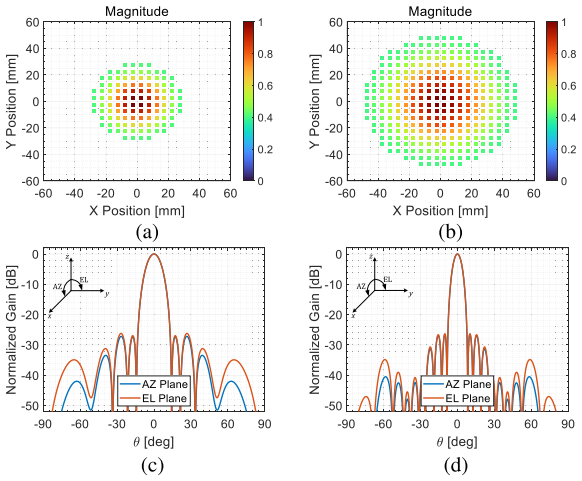

FIGURE 7. Slotted array antenna model and its radiation pattern (a, b) Slot position and feed magnitude of array 1 and 2 (D = 60, 100 mm) (c, d) Ideal radiation pattern of array 1 and 2. (HPBW = 11°, 6.6°, and SLL = −26.2, 26.4 dB.)

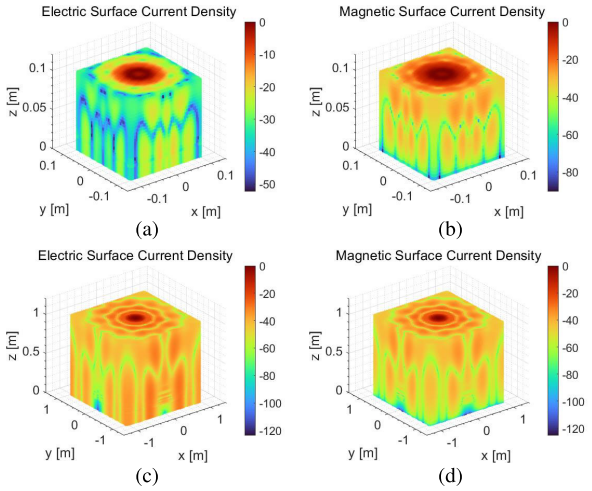

FIGURE 8. Equivalent surface current density of boundary box in array 1 (a, b) Boundary box size is 0.2 m (c, d) Boundary box size is 2.0 m.

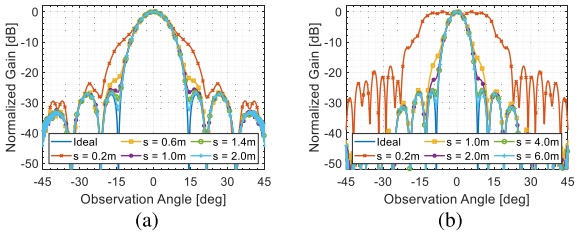

FIGURE 9. Radiation pattern for different sizes of the boundary box (a) Array 1 (b) Array 2.

point $\vec{r}_{b,n}$, $R_{b,n}$ is the magnitude of $\vec{R}_{b,n}$ and $\hat{R}_{b,n}$ is the normalized vector of $\vec{R}_{b,n}$. Assuming that the boundary mesh consists of intervals of less than half a wavelength for high accuracy and a total of N squares, the integral expression of eqs. (7) can be expressed discretely by

$$\vec{E}_s(\vec{r}_{b,n}) = \frac{jkc^2}{4\pi}\sum_{n}^{N}[\hat{R}_{b,n}\times\hat{R}_{b,n}\times\vec{J}_{b,n}(\vec{r}_{b,n}) + \hat{R}_{b,n}\times\vec{M}_{b,n}(\vec{r}_{b,n})]\frac{e^{-jkR_{b,n}}}{R_{b,n}} \quad (8)$$

where c is the spacing between the boundary meshes. Since the boundary mesh consists of squares, its area is calculated as c^2.

III. NUMERICAL RESULTS

In order to calculate the radiation pattern of the antenna covered with FSS, it is necessary to model the antenna, FSS, and boundary box to be used in the analysis. Therefore, this section introduces the model to be used for analysis.

A. ANTENNA MODELING

The antenna to be used for analysis was modeled as two arrays, array 1 and array 2, as shown in Fig. 7. The array was designed using taylor tapered distribution, and the side lobe level (SLL) limit was set to −25 dB, and nbar is 3. Taylor tapered distribution was implemented using MATLAB phased array antenna toolbox. The spacing between arrays is $0.5\lambda_0$, and it was analyzed at a frequency f_0 of 30 GHz. In addition, the ideal radiation pattern of the antenna was calculated using Eqs. (2), and the location of the observation point was set very far from the source.

Array 1 is modeled as a circular slotted array antenna with 112 elements, and has a diameter (D) of 60mm. (See Fig. 7a) The radiation pattern of array 1 is shown for the azimuth (AZ) and elevation (EL) planes as shown in Fig. 7c. In the AZ and EL planes, the half power beam width (HPBW) is 11°, and the SLL is −26.2 dB. The array 2 has 316 elements and has a diameter (D) of 100mm. (See Fig. 7b) As shown in Fig. 7d, both AZ and EL planes have HPBW of 6.6° and SLL of −26.2 dB.

B. BOUNDARY BOX SIZE

To analyze the relationship between the size of the boundary box and the radiation pattern, we compared and analyzed boundary boxes of different sizes. When the number of sources is 112 (array 1), the normalized surface current density ($\vec{J}_b$) is compared for the case where the boundary size is 0.2 and 2 m, respectively, as shown in Fig. 8. In Fig. 8c, the boundary size is 0.2 m, the distance from the array aperture is about 0.1 m (same as Size/2). In this case, you can see that the surface current density is concentrated in the center of the beam in the upper plane. On the other hand, when the boundary size is 2 m as shown in Fig. 8d, it is confirmed that a null is formed on the top surface. It implies that even with the same array, the radiation pattern can be different depending on the boundary size.

The radiation pattern change according to the size of the boundary box of array 1 and array 2 is shown as Fig. 9. The label in Fig. 9 represents the distance (same

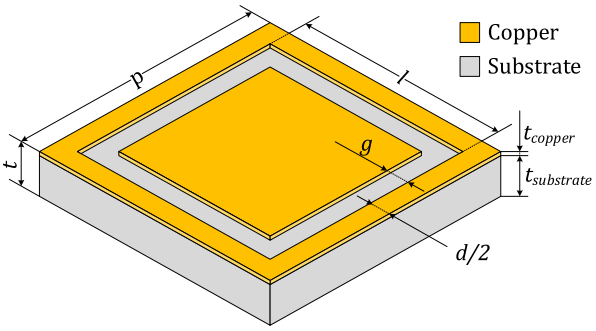

FIGURE 10. Square ring unit cell of the FSS layer.

as Size/2) between the boundary box and the antenna aperture. As observed in the previous Fig. 8c, when the distance between the apertures is 0.1 m, the null in the beam is not well delineated. When a distance of about 0.7 m or more, the first null becomes clear. This phenomenon was also observed in array 2. The first null in array 2 was observed when the distance was greater than about 2 m.

We calculated the field using the far-field approximation equation for the rays generated by the slot antenna. The far-field approximation introduces a phase error, and the distance at which this error becomes smaller is called the Rayleigh distance. Rayleigh distance, known as the far field condition, is the distance at which this phase error below $\pi/8$ [30]. The Rayleigth distance r_R is defined by

$$r_R = \frac{s}{2} = \frac{2D^2}{\lambda_0} \tag{9}$$

where λ_0 is the wavelength of the analysis frequency f_0. In the case of array 1, since D = 60 mm, a distance of 0.7 m or more, and array 2, D = 100 mm, a distance of 2.0 m or more must be secured to satisfy the far field condition. Therefore, the size of the boundary should be set to satisfy the Rayleigh distance according to the diameter of the antenna.

C. FREQUENCY SELECTIVE SURFACE

The FSS to be used for calculation and analysis is composed of a simple rectangular slot as shown in Fig. 10. FSS consists of copper and substrate, and the substrate is modeled with Rogers Duroid 5880 with a thickness of $t_{substrate} = 0.254$ mm, $\epsilon_r = 2.2$, and $\tan\delta = 0.0009$. The design parameters of the FSS consisted of the length l of the rectangular loop, the width g of the slot, the spacing d between the periodic structures, and the size $p = d + l$ of the periodic structures. We designed a FSS that is well matched at 30 GHz and a mismatched FSS that resonates at 22.2 GHz to analyze the change in the radiation pattern according to the characteristics of the FSS. Matched FSS has parameters l = 2.36 mm, g = 0.15 mm, d = 0.4 mm, and p = 2.76 mm. Mismatched FSS has l = 3 mm, p = 3.44 mm, and g and d are the same as matched FSS. The reflection and transmission characteristics of FSS are shown in Fig. 11. For matched FSS, it can be seen that it

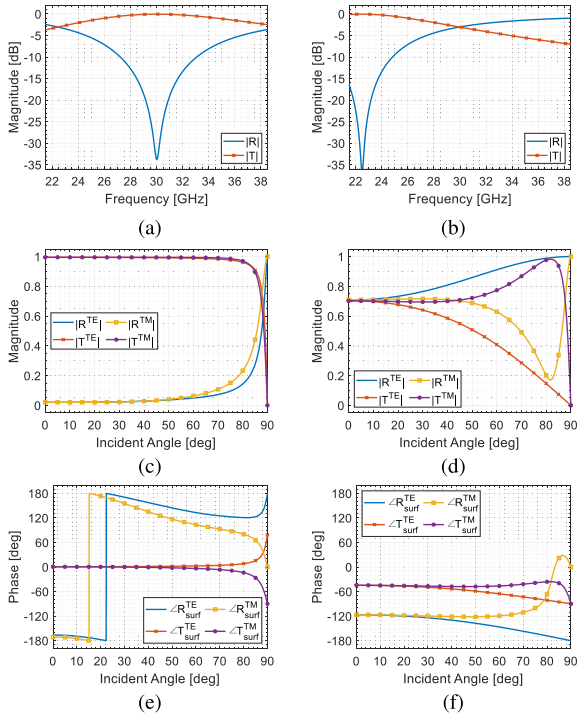

FIGURE 11. Reflection and transmission coefficients of FSS (a, b) Versus frequency for good and mismatched FSS, (c, d) Magnitude versus incident angle for good and mismatched FSS at 30 GHz, and (e, f) Phase versus incident angle for good and mismatched FSS at 30 GHz.

resonates at 30 GHz in Fig. 11a. In addition, it has a relatively low reflection coefficient and a high transmission coefficient even at a high incidence angle of 60° or more at 30 GHz in Fig. 11e. On the other hand, the mismatched FSS resonates at 22.2 GHz, so it has a low reflection and transmission coefficient of −3dB at 30 GHz in 11b. In addition, as the incident angle changes at 30 GHz, it shows different characteristics for each polarization in 11f. As the angle of incidence increases, the reflection coefficient of TE polarization increases and that of TM polarization decreases. Conversely, as the angle of incidence increases, the transmission coefficient of TE polarization decreases and that of TM polarization increases.

D. ANALYSIS RESULTS

We calculated the radiation patterns of array antennas covered with matched and mismatched of FSS. It was modeled in the same shape as Fig 1, and the distance h between the antenna and the FSS was set to 10 mm. The size D of FSS and antenna is 100 mm, and the antenna array 2 model was used. The size of the boundary box was set to 3.0 m to sufficiently satisfy the far field condition. The result of calculating the radiation pattern under these conditions is shown in Fig. 12. Matched FSS has low reflection and high transmission, so almost no pattern distortion is observed compared to Fig. 9b. On the other hand, in the case of the mismatched FSS, the loss in the main beam is noticeable due to the relatively high transmission loss. It also has a high reflection coefficient, so ripples are observed at the side lobe. This is strongly observed in

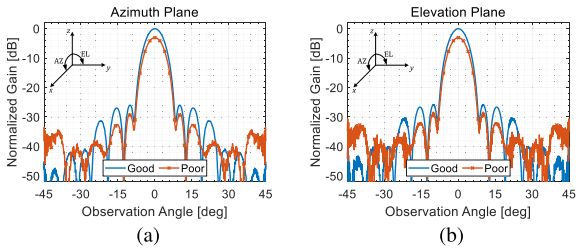

FIGURE 12. Radiation pattern of array 2 covered with good and mismatched FSS (a) On azimuth plane (b) On elevation plane.

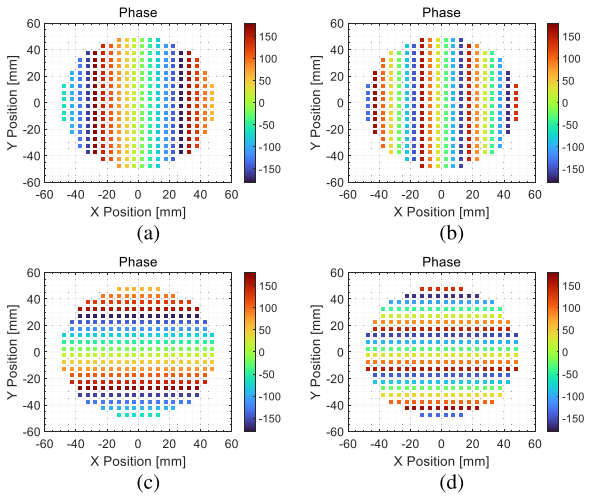

FIGURE 13. Phase of each element for beam steering. (a, b) 10, 20 degree steering in azimuth direction (c, d) 10, 20 degree steering in elevation direction.

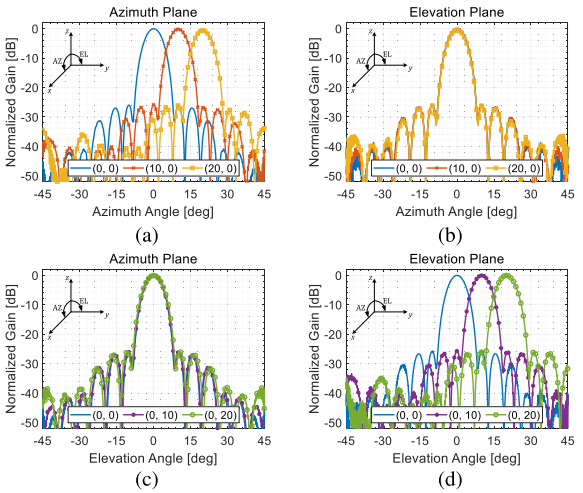

FIGURE 14. Radiation pattern calculation result according to beam steering (a, b) The azimuth, elevation cut of the radiation pattern in azimuth direction steering (c, d) The azimuth, elevation cut of the radiation pattern in elevation direction steering.

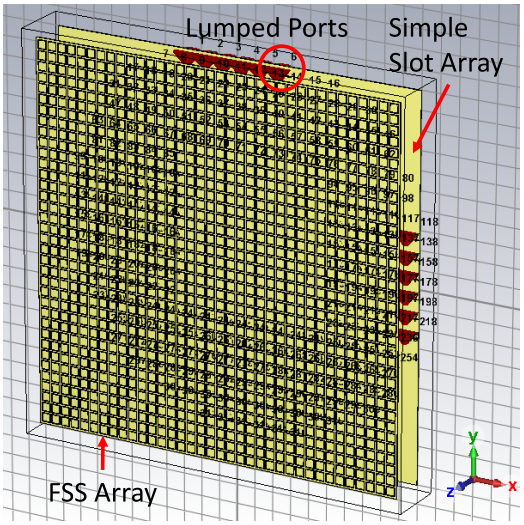

FIGURE 15. CST simulation setup for verification. A FSS is mounted on an array antenna consisting of an array of slots excited by a lumped port.

the elevation plane where the influence of TE polarization is large. The result show that the radiation pattern distortion is small when covering the low reflection and high transmission FSS.

The radiation pattern according to the beam steering angle was analyzed using the proposed technique. The antenna in Fig. 7a was used, and the radiation patterns were calculated when steering 10 degrees and 20 degrees in the AZ and EL directions. The phase of each antenna element for beam steering is shown in Fig. 13. Depending on the steering direction, each row or column has a certain phase difference. The result of calculating the radiation pattern by applying the matched FSS is shown in Fig. 14. The legend in Fig. 14, the first number in parentheses indicates the steering angle in the azimuth direction, and the second number indicates the steering angle in the elevation direction. When the beam is steered at 10 degrees and 20 degrees in the azimuth direction (see Fig. 14a, 14b, the main beam losses are -0.19 and -0.58 dB, respectively, and the main beam loss increases as the steering angle increases. On the other hand, when the beam is steered in the elevation direction (see Fig. 14c, 14d), the main beam loss is -0.053 and -0.038 dB, respectively, and no obvious main beam loss according to the steering angle is observed. When the slot antenna is placed as shown in Fig. 4, null exists in the azimuth direction. Therefore, the larger the steering angle, the greater the main beam loss regardless of the FSS.

E. SIMULATIONS FOR VALIDATION

To validate and compare our proposed method, we performed CST studio suite simulation as shown in Fig. 15. Problem geometry and dimensions used for the CST simulations are identical to those depicted in Fig. 1. The analysis frequency f_0 was 30 GHz, and the size D of the FSS and antenna was set to 100 mm, with the spacing h set to 10 mm. A lumped port was installed between the slots to radiate the port of each antenna element. The simulation was conducted using the finite integration technique (FIT) [31], one of the EM simulation solvers of the CST studio suite.

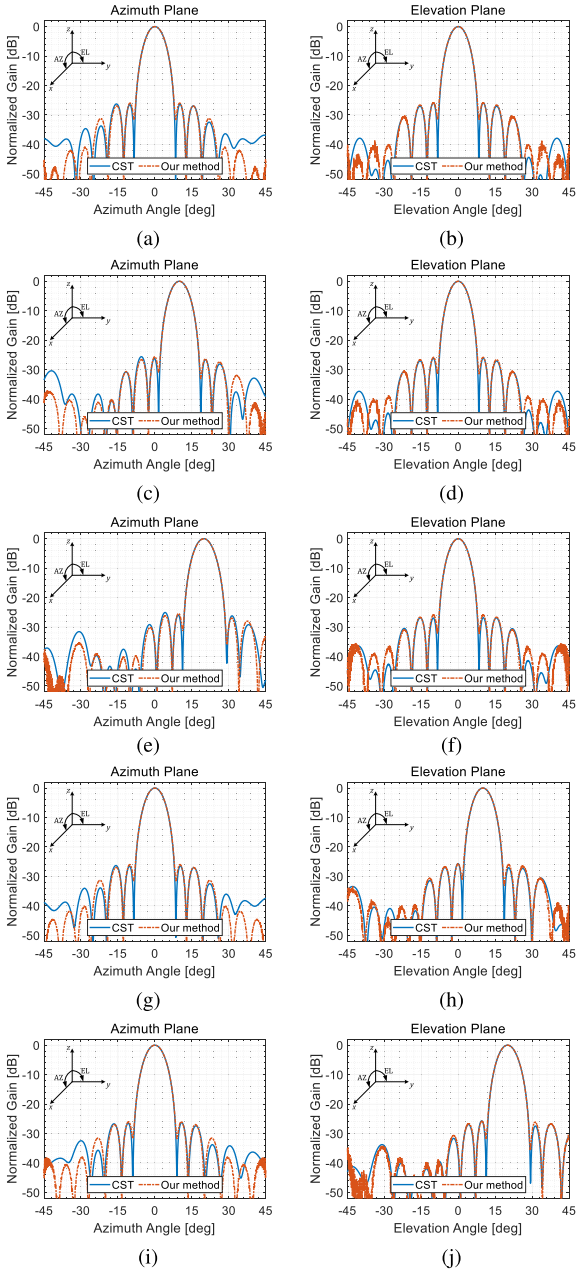

FIGURE 16. Comparison of normalized gain in azimuth and elevation planes between CST and proposed method in 316 slot array antennas covered by matched of FSS (a, b) No beam steering (c, d) azimuth steering of 10° (e, f) azimuth steering of 20° (g, h) elevation steering of 10° (i, j) elevation steering of 20°.

To validate our proposed method, we simplified the circuit configuration by using a lumped port for each slot to allow all array elements to radiate. We did not include detailed circuits in our simulation to focus on evaluating the performance of the proposed method. To validate and compare our proposed method, we performed CST studio suite simulation as shown in Fig. 15. The magnitude and phase supplied to each port were set the same as in the previous analysis. Results obtained by using the CST studio and the proposed method are compared in Fig. 16. The calculation took approximately 39 hours, using about 30 million meshes and 24.7 GB of memory.

F. DISCUSSION

The Table 1 summarizes the contents of the experiment, errors, calculation time, and memory consumption. In terms of calculation time, the proposed model is divided into the process of calculating the surface current density (sections II-B to II-E) and the radiation pattern according to the observation point (section II-F). In the case of the radiation pattern, it is the calculation time required when outputting 0.1 degree intervals from AZ and EL plane −45 to 45 degrees (total 901 points), and this process was calculated with CPU and GPU, respectively.

Error is calculated as root mean square error (RMSE) and is defined by

$$\text{Error} = \sqrt{\frac{1}{N_{obs}} \sum_{i \in [\theta_{obs}]}^{N_{obs}} \left(\text{predict}_i - \text{ideal}_i\right)^2} \tag{10}$$

where θ_{obs} is the observation angle and N_{obs} is the total number of observation points. The error was calculated by using a linear scale to compare predicted and ideal values. The range of the observation angle was set from the main beam to the third null. This is because the values after that vary greatly depending on the analysis method. First, the value of Fig. 9 was used for the predict value, and the error was calculated using the value of Fig. 7 for the ideal value. It can be seen that as the boundary size increases (that is, the far field condition is satisfied), the error decreases. In Fig. 16, the error was calculated for the AZ and EL planes by adopting our method value as the predict value and the CST value as the ideal value. As a result, it shows errors of up to 5.62E-3, 2.16E-3, which means that the radiation characteristics can be calculated efficiently.

For the calculations, we used a personal computer equipped with AMD Ryzen 9 5950X CPU (16 cores, 32 threads, 3.4 GHz), NVIDIA RTX 3090 GPU, and 128 GB of memory. The workstation running CST has AMD Ryzen Threadripper PRO 5995WX CPU (64 cores, 128 threads, 2.7 GHz), NVIDIA A100 GPU, and 512 GB of memory installed. Although it is difficult to make a fair comparison because the performance of the computers used is different (workstation is better), our method has a faster computation speed and consumes less memory than the full-wave method.

Our method requires a significant amount of memory to allocate the boundary mesh, which is a 2D surface. As the size of the boundary box being analyzed increases, memory usage increases proportionally to the square of the size. Calculation time is also proportional to the square of the boundary size and the number of antennas. To reduce calculation time, we used openMP-based CPU parallel processing and CUDA Thrust-based GPU parallel processing techniques. However, in the case of the GPU, larger boundary sizes lead to faster speed improvements due to reduced data transfer time between the GPU and CPU. We could also consider using

TABLE 1. Summary of analysis and calculation results.

Purpose	Derivation	Result (AZ, EL Plane)	Calculation Time			Consumed Memory	Boundary Size S	# of Elements & Diameter D	Beam Steering	Material Type
			Surface Current Density	Radiation Pattern (901 points)						
			CPU	CPU	GPU					
Analysis of the relationship between boundary box size and radiation pattern (Fig. 9)	The boundary size that satisfies the far field condition must be set. $S \geq \frac{2D^2}{\lambda_0}$	Error = 64.5E-3 (only AZ)	0.09 s	0.22 s	1.21 s	11.0 MB	0.2 m (20 λ)	112 60 mm (6 λ)	AZ = 0° EL = 0°	Free-space
		Error = 4.53E-3 (only AZ)	0.55 s	1.92 s	3.81 s	25.4 MB	0.6 m(60 λ)			
		Error = 1.88E-3 (only AZ)	1.49 s	5.35 s	5.11 s	52.9 MB	1.0 m (100 λ)			
		Error = 1.03E-3 (only AZ)	2.92 s	10.4 s	6.99 s	93.8 MB	1.4 m (140 λ)			
		Error = 0.80E-3 (only AZ)	5.91 s	21.4 s	11.4 s	180.9 MB	2.0 m (200 λ)			
		Error = 593E-3 (only AZ)	0.24 s	0.26 s	1.14 s	11.5 MB	0.2 m (20 λ)	316 100 mm (10 λ)	AZ = 0° EL = 0°	
		Error = 17.3E-3 (only AZ)	4.05 s	5.35 s	5.29 s	52.8 MB	1.0 m (100 λ)			
		Error = 3.77E-3 (only AZ)	16.1 s	21.3 s	11.2 s	181.4 MB	2.0 m (200 λ)			
		Error = 0.86E-3 (only AZ)	64.5 s	85.4 s	32.3 s	696.1 MB	4.0 m (400 λ)			
		Error = 0.34E-3 (only AZ)	145 s	193 s	67.4 s	1,554 MB	6.0 m (600 λ)			
Radiation pattern analysis by FSS type (Fig. 12)	High transmittance and low reflectance FSS prevent radiation pattern distortion.	Loss = -0.05, -0.05 dB SLL = 25.93, 25.63 dB HPBW = 6.48°, 6.46°	145 s	194 s	66.0 s	1,554 MB	6.0 m (600 λ)	316 100 mm (10 λ)	AZ = 0° EL = 0°	Good type FSS
		Loss = -3.08, -3.08 dB SLL = 25.84, 24.73 dB HPBW= 6.54°, 6.48°	145 s	193 s	66.7 s	1,554 MB	6.0 m (600 λ)			Poor type FSS
Radiation pattern analysis by beam steering (Fig. 14)	Main beam loss occurs when the beam is steered in the azimuth direction due to the radiation pattern of a single element.	Loss = -0.19, -0.19 dB SLL = 25.61, 25.77 dB HPBW= 6.48°, 6.48°	146 s	192 s	66.6 s	1,554 MB	6.0 m (600 λ)	316 100 mm (10 λ)	AZ = 10° EL = 0°	Good type FSS
		Loss = -0.58, -0.58 dB SLL = 25.34, 25.62 dB HPBW= 6.56°, 6.48°	144 s	191 s	66.5 s	1,554 MB	6.0 m (600 λ)		AZ = 20° EL = 0°	
		Loss = -0.05, -0.05 dB SLL = 25.95, 25.78 dB HPBW= 6.48°, 6.52°	144 s	191 s	66.3 s	1,554 MB	6.0 m (600 λ)		AZ = 0° EL = 10°	
		Loss = -0.04, -0.04 dB SLL = 25.96, 25.76 dB HPBW= 6.88°, 6.84°	145 s	193 s	66.3 s	1,554 MB	6.0 m (600 λ)		AZ = 0° EL = 20°	
Validation (Fig. 16)	Confirm good agreement, reduced computing resources.	Error = 1.62E-3, 1.64E-3	≈ 39 h (CST) (Mesh Cells: 30,398,130) (Our method: ≈ 210 s)			≈ 24.7 GB (Our method: ≈1.6 GB)	-	316 100 mm (10 λ)	AZ = 0° EL = 0°	Good type FSS
		Error = 4.02E-3, 1.71E-3							AZ = 10° EL = 0°	
		Error = 5.62E-3, 2.16E-3							AZ = 20° EL = 0°	
		Error = 1.54E-3, 2.33E-3							AZ = 0° EL = 10°	
		Error = 1.56E-3, 1.58E-3							AZ = 0° EL = 20°	

efficient algorithms for collecting sampling points to further reduce computation time.

On the other hand, when using a full-wave method with a 3D structure mesh, memory consumption is expected to

increase proportionally to the cube of the size. This is because the number of meshes increases in proportion to the third power as the size being analyzed increases. The larger the number of meshes, the more memory and time required. Therefore, our proposed method will be more efficient than the full-wave method as the size of the problem being analyzed increases.

Note that the size of each slot is 4.6 mm (0.46 λ), and the far field distance of each slot is 4.2 mm (0.42 λ) calculated by $2D^2/\lambda$. Therefore, the distance between slot and FSS satisfies the far field condition (h = 10 mm in Fig. 1). Also, our proposed method is expected to be applicable to frequencies below 30 GHz if the distance between slot and FSS satisfies the far field condition.

The proposed method can also analyze non-planar structures, such as curved surfaces, but it may be computationally inefficient. Regarding structures different from planar FSS structures, the modeling of non-planar curved surfaces often involves numerous meshes. In this case, applying the image method to find the ray path may be computationally inefficient. When the number of meshes is large, it is more efficient to apply a tree data structure algorithm such as boundary volume hierarchy. This algorithm is used to search for intersections of rays and meshes, and it is efficient for large amounts of meshes.

The antenna that can be arranged can represent other antennas as well as slot antennas. However, in this case, near field information on the $\vec{E}$ and $\vec{H}$ fields of the analyzed antenna is required for accuracy, which can be described as far field characteristics using the surface equivalence principle and eqs. (2).

Finally, we assumed that the specular reflection and transmission occur in the medium. Therefore, the analysis may not be valid when diffuse due to rough surfaces or higher order modes due to unit structures larger than the half wavelength occur. When analyzing these materials, additional modeling of the ray mechanism will be required.

Even with these limitations, the proposed method can efficiently analyze the change in the radiation pattern of the antenna due to FSS.

IV. CONCLUSION

A method for calculating the antenna radiation characteristics inside the planar FSS cover based on the ray tracing method and PO was proposed. The image method for determining the direct or transmited, and multiple reflected ray paths between the antenna and the FSS is described. We set the boundary box consisting of a boundary mesh spaced less than 0.5 λ, and found the path of the rays reaching the boundary mesh. By calculating the radiation patterns of 112 and 316 slot antennas, it was confirmed that the size of the boundary box must satisfy the far field condition. In addition, it was confirmed that the antenna radiation characteristic distortion was small only when the low reflection and high transmission FSS were used. The proposed technique was verified by comparison with a commercial simulator. Furthermore, it was shown that the proposed technique can efficiently calculate the radiation with few computational resource. The proposed method can be used to analyze the effect of the antenna radiation pattern due to the FSS cover and radome.

REFERENCES

[1] B. Philips, "Ray tracing analysis of the transmission performance of curved FSS," *IEE Proc. Microw., Antennas Propag.*, vol. 142, no. 3, p. 193, 1995, doi: 10.1049/ip-map:19951896.

[2] H.-S. Lee and H. Park, "Prediction of radome bore-sight errors using a projected image of source distributions," *Prog. Electromagn. Res.*, vol. 92, pp. 181–194, 2009.

[3] J. H. Kim, H. J. Chun, I. P. Hong, Y. J. Kim, and Y. B. Park, "Analysis of FSS radomes based on physical optics method and ray tracing technique," *IEEE Antennas Wireless Propag. Lett.*, vol. 13, pp. 868–871, 2014.

[4] J. Kim, S. Lee, H. Shin, K.-Y. Jung, H. Choo, and Y. Park, "Radiation from a cavity-backed circular aperture array antenna enclosed by an FSS radome," *Appl. Sci.*, vol. 8, no. 12, p. 2346, Nov. 2018. [Online]. Available: https://www.mdpi.com/2076-3417/8/12/2346

[5] J. Kim, S. C. Song, H. Shin, and Y. B. Park, "Radiation from a millimeter-wave rectangular waveguide slot array antenna enclosed by a Von Karman radome," *J. Electromagn. Eng. Sci.*, vol. 18, no. 3, pp. 154–159, 2018.

[6] H. Shin, D. Yoon, K. Choi, I. Jung, and Y. B. Park, "Analysis of a curved multi-layer radome using a flat model and the ray tracing technique," *J. Electr. Eng. Technol.*, vol. 15, no. 2, pp. 787–794, Mar. 2020.

[7] H. Shin, D. Yoon, D.-Y. Na, and Y. B. Park, "Analysis of radome cross section of an aircraft equipped with a FSS radome," *IEEE Access*, vol. 10, pp. 33704–33712, 2022.

[8] V. K. Kanth and S. Raghavan, "EM design and analysis of frequency selective surface based on substrate-integrated waveguide technology for airborne radome application," *IEEE Trans. Microw. Theory Techn.*, vol. 67, no. 5, pp. 1727–1739, May 2019.

[9] W. Liao, W. Zhang, Y. Hou, S. Chen, C. Y. Kuo, and M. Chou, "An FSS-integrated low-RCS radome design," *IEEE Antennas Wireless Propag. Lett.*, vol. 18, no. 10, pp. 2076–2080, Oct. 2019.

[10] I.-G. Lee, W.-S. Oh, Y. J. Kim, and I.-P. Hong, "Design and fabrication of absorptive/transmissive radome based on lumped elements composed of hybrid composite materials," *IEEE Access*, vol. 8, pp. 129576–129585, 2020.

[11] L. Zhou and Z. Shen, "Hybrid frequency-selective rasorber with low-frequency diffusion and high-frequency absorption," *IEEE Trans. Antennas Propag.*, vol. 69, no. 3, pp. 1469–1476, Mar. 2021.

[12] L. Wang, S. Liu, X. Kong, Q. Yu, X. Zhang, and H. Zhang, "A multifunctional hybrid frequency-selective rasorber with a high-efficiency cross-polarized passband/Co-polarized specular reflection band," *IEEE Trans. Antennas Propag.*, vol. 70, no. 9, pp. 8173–8183, Sep. 2022.

[13] S. C. Bakshi, D. Mitra, and F. L. Teixeira, "Multifunctional frequency selective rasorber with dual mode and continuous tunability," *IEEE Trans. Antennas Propag.*, vol. 69, no. 9, pp. 5704–5715, Sep. 2021.

[14] S.-K. Kim, G.-T. Lee, and I.-S. Seo, "Design of AEM FSS-radome for array antenna," *J. Korean Inst. Electromagn. Eng. Sci.*, vol. 22, no. 12, pp. 1180–1183, Dec. 2011, doi: 10.5515/kjkiees.2011.22.12.1180.

[15] B. Liu, Z. Nie, Y. Cao, H. Gu, K. Fan, and Y. Sui, "Performance improvement by new integration scheme of Radome-FSS-Antenna," in *Proc. IEEE Int. Conf. Comput. Electromagn. (ICCEM)*, Mar. 2018, pp. 1–3.

[16] H. F. Álvarez, D. A. Cadman, A. Goulas, M. E. de Cos Gómez, D. S. Engstrøm, J. C. Vardaxoglou, and S. Zhang, "3D conformal bandpass millimeter-wave frequency selective surface with improved fields of view," *Sci. Rep.*, vol. 11, no. 1, pp. 1–12, Jun. 2021, doi: 10.1038/s41598-021-91218-y.

[17] M. Bilal, R. Saleem, Q. H. Abbasi, B. Kasi, and M. F. Shafique, "Miniaturized and flexible FSS-based EM shields for conformal applications," *IEEE Trans. Electromagn. Compat.*, vol. 62, no. 5, pp. 1703–1710, Oct. 2020.

[18] Z. Yun and M. F. Iskander, "Ray tracing for radio propagation modeling: Principles and applications," *IEEE Access*, vol. 3, pp. 1089–1100, 2015.

[19] L. Tian, V. Degli-Esposti, E. M. Vitucci, and X. Yin, "Semi-deterministic radio channel modeling based on graph theory and ray-tracing," *IEEE Trans. Antennas Propag.*, vol. 64, no. 6, pp. 2475–2486, Jun. 2016.

[20] F. A. Agelet, A. Formella, J. M. H. Rabanos, F. I. D. Vicente, and F. P. Fontan, "Efficient ray-tracing acceleration techniques for radio propagation modeling," *IEEE Trans. Veh. Technol.*, vol. 49, no. 6, pp. 2089–2104, Nov. 2000.
[21] T. E. Athanaileas, G. E. Athanasiadou, G. V. Tsoulos, and D. I. Kaklamani, "Parallel radio-wave propagation modeling with image-based ray tracing techniques," *Parallel Comput.*, vol. 36, no. 12, pp. 679–695, Dec. 2010.
[22] H. Ling, R.-C. Chou, and S.-S. Lee, "Shooting and bouncing rays: Calculating the RCS of an arbitrarily shaped cavity," *IEEE Trans. Antennas Propag.*, vol. 37, no. 2, pp. 194–205, Feb. 1989.
[23] Y. Tao, H. Lin, and H. Bao, "GPU-based shooting and bouncing ray method for fast RCS prediction," *IEEE Trans. Antennas Propag.*, vol. 58, no. 2, pp. 494–502, Feb. 2010.
[24] H. Shin, D. Yoon, D.-Y. Na, and Y. B. Park, "Analysis of transmission loss and boresight error of a curved FSS radome-enclosed antenna," *IEEE Access*, vol. 9, pp. 95843–95852, 2021.
[25] J.-I. Lee and D.-W. Seo, "Improvement of computational efficiency for fast ISAR image simulation through nonuniform fast Fourier transform," *IEEE Antennas Wireless Propag. Lett.*, vol. 20, no. 12, pp. 2402–2406, Dec. 2021.
[26] Y.-B. Tao, H. Lin, and H. J. Bao, "KD-tree based fast ray tracing for RCS prediction," *Prog. Electromagn. Res.*, vol. 81, pp. 329–341, 2008.
[27] X.-Y. He, X.-B. Wang, X. Zhou, B. Zhao, and T.-J. Cui, "Fast ISAR image simulation of targets at arbitrary aspect angles using a novel SBR method," *Prog. Electromagn. Res. B*, vol. 28, pp. 129–142, 2011.
[28] S. Suk, T.-I. Seo, H.-S. Park, and H.-T. Kim, "Multiresolution grid algorithm in the SBR and its application to the RCS calculation," *Microw. Opt. Technol. Lett.*, vol. 29, no. 6, pp. 394–397, Jun. 2001.
[29] R. J. Burkholder and T.-H. Lee, "Adaptive sampling for fast physical optics numerical integration," *IEEE Trans. Antennas Propag.*, vol. 53, no. 5, pp. 1843–1845, May 2005.
[30] W. C. Chew, *Lecture on Electromagnetics Field Theory*. West Lafayette, IN, USA: Purdue Univ., Fall 2020.
[31] M. Clemens and T. Weiland, "Discrete electromagnetism with the finite integration technique," *Prog. Electromagn. Res.*, vol. 32, pp. 65–87, 2001, doi: 10.2528/pier00080103.

DAEYEONG YOON (Student Member, IEEE) received the B.S. degree in electrical and computer engineering from Ajou University, Suwon, South Korea, in 2018, where he is currently pursuing the integrated M.S./Ph.D. degree in AI convergence network. His research interests include periodic structure, frequency selective surface, radomes, and radar cross section.

JIHYUNG KIM (Member, IEEE) received the B.S. and integrated M.S./Ph.D. degree in electrical and computer engineering from Ajou University, Suwon, South Korea, in 2009 and 2016, respectively. Since 2016, he has been a Researcher with Hanwha Systems, Yongin, South Korea. His research interests include the analysis of aperture array antennas and radomes.

HOKEUN SHIN (Member, IEEE) received the B.S. degree in electrical and computer engineering and the integrated M.S. and Ph.D. degree in AI convergence network from Ajou University, Suwon, South Korea, in 2015 and 2021, respectively. From 2021 to 2023, he was a Senior Engineer with Hanwha Systems, Seongnam, South Korea. He joined the Core Component Technology Team of Mobile Experience, Samsung Electronics, Suwon, in 2023, where he is currently a Staff Engineer. His research interests include antennas, EMI/EMC, high-frequency techniques, frequency selective surface, radomes, and radar cross section.

DONG-YEOP NA (Member, IEEE) received the B.S. and M.S. degrees in electrical and computer engineering from Ajou University, Suwon, South Korea, in 2012 and 2014, respectively, and the Ph.D. degree in electrical and computer engineering from The Ohio State University, Columbus, OH, USA, in 2018. From 2019 to 2022, he was with the Elmore Family School of Electrical and Computer Engineering, Purdue University, West Lafayette, IN, USA, as a Postdoctoral Research Associate and a Research Scientist. He joined the Department of Electrical Engineering, Pohang University of Science and Technology, Pohang, South Korea, in 2022, where he is currently an Assistant Professor. His research interests include computational electromagnetics, kinetic plasma modeling via particle-in-cell algorithm, and quantum electromagnetics.

YONG BAE PARK (Senior Member, IEEE) received the B.S., M.S., and Ph.D. degrees in electrical engineering from the Korea Advanced Institute of Science and Technology, South Korea, in 1998, 2000, and 2003, respectively. From 2003 to 2006, he was with the Korea Telecom Laboratory, Seoul, South Korea. He joined the School of Electrical and Computer Engineering, Ajou University, South Korea, in 2006, where he is currently a Professor. His research interests include electromagnetic field analysis, high-frequency methods, metamaterial antennas, radomes, and stealth technology.